Engineering with Computers (2009) 25:25–36
DOI 10.1007/s00366-008-0110-5

ORIGINAL ARTICLE

Automated adaptive cardiovascular flow simulations

Onkar Sahni · Kenneth E. Jansen · Charles A. Taylor · Mark S. Shephard

Received: 3 March 2007 / Accepted: 17 October 2007 / Published online: 31 October 2008

Abstract We present an automatic adaptive procedure to perform blood flow simulations in the cardiovascular system. The procedure allows the user to start with subject-specific data collected through clinical measurements, like magnetic resonance imaging (MRI) data, and evaluate physiological parameters of interest, like flow distribution, pressure variations, wall shear stress, in an automatic and efficient manner. The process involves construction of geometric models of blood vessels, specification of flow conditions and application of an adaptive flow solver. The latter is based on incompressible Navier–Stokes equations using adaptive spatial discretization (meshing) techniques. In this article, we demonstrate the method on a model of a human abdominal aorta of a normal subject with geometry and flow rates assimilated from MRI data. The results obtained show that boundary layer mesh adaptivity offers a better alternative leading to more accurate predictions, especially for key physiological quantities like wall shear stress.

Keywords Blood flow simulations · Computational fluid dynamics · Adaptive meshing techniques · Cardiovascular flow simulations

O. Sahni (✉) · K. E. Jansen · M. S. Shephard
Scientific Computation Research Center, Rensselaer Polytechnic Institute, Troy, NY 12180, USA
e-mail: osahni@scorec.rpi.edu

K. E. Jansen
e-mail: kjansen@scorec.rpi.edu

M. S. Shephard
e-mail: shephard@scorec.rpi.edu

C. A. Taylor
E350 Clark Center, Stanford University, 318 Campus Drive, Stanford, CA 94305, USA
e-mail: taylorca@stanford.edu

1 Introduction

A range of techniques, including analytical, experimental and computational, have been used to quantify flow conditions within the cardiovascular system in order to understand its functioning and in diagnosing and treating cardiovascular diseases (e.g., see [1, 2]). In recent years, computational methods have been used extensively in simulating blood flows within three-dimensional models of arteries to evaluate flow parameters in subject-specific anatomic and physiologic models. Application of computational techniques allows one to predict physiologic parameters of interest in detail, which can be used to design improved treatment strategies [3–6] and medical devices that mimic or alter blood flow [7].

Remarkable progress has been made in constructing realistic anatomical models from three-dimensional medical imaging data. Such anatomic data, supported by relevant physiologic information including flow rate and distribution at inlets and outlets, are utilized to adequately account for boundary conditions in performing flow computations. Incorporating further complex phenomena of arterial wall motion, wall mechanical properties and cellular-level interactions is underway [8–10].

The vast extent and complexity of the cardiovascular system coupled with limits imposed by current computing and imaging technologies for practical purposes preclude a three-dimensional representation of the system including smaller arteries, capillaries, veins etc. Hence, we constrain the modeling of blood flow to major arteries based on transient, incompressible Navier–Stokes equations, assuming Newtonian constitutive behavior with rigid and impermeable vessel walls, and model the downstream vascular bed with the help of adequate outflow boundary conditions to obtain physiologic flow conditions [11].

The reliability of numerical simulation depends on the spatial discretization of the physical domain, i.e., on the process of subdividing the domain into a finite number of elements, also referred to as the mesh. For problems involving subject-specific anatomic models the amount of mesh resolution required for a certain level of accuracy is unknown a priori. Increasing the mesh resolution in an uniform global fashion for practical problems would lead to excessive demands on computational resources and may turn out to be prohibitive.

In order to expedite the performance of numerical computations, resolution within the discretization needs to be applied in a local fashion. In this scenario, it is desirable to apply a procedure where the quality of the computed solution on an existing discretization, that is evaluated based on a posteriori measures and/or indicators of the error, is used to drive improvements to the local resolution, which in turn enrich the solution approximation. Moreover, in the case of viscous flow simulations like blood flows, meshes with layered and graded elements near vessel walls, commonly known as boundary layer meshes [12], provide more accurate results for key wall quantities, like wall shear stress [13]. Pre-defined boundary layer meshes have been used for cases with prior knowledge of solution features but the deficiency involved is twofold for practical cases; the process can be tedious and requires expertise in terms of knowledge about the solution that is often not available. Hence, automatic and adaptive construction of properly configured (boundary layer) meshes is central to the ability to effectively perform these simulations.

The organization of the paper is as follows. It begins with the description of the overall adaptive process. We then demonstrate the capability of the method by applying it to a subject-specific model of a healthy human abdominal aorta involving geometry and flow rates generated from MRI data [14]. For this purpose we quantify spatial distribution of pressure and wall shear stress along with temporal variations in flow rate and pressure at various outlets.

2 Overall adaptive process

In this section, we describe the overall automatic and adaptive approach to simulate cardiovascular flows. The process is initiated based on the three-dimensional imaging data obtained through MRI [14]. Subject-specific anatomic data is used to construct three-dimensional geometric models of the patient's vasculature. Physiologic information is extracted to form models for governing equations, boundary and initial conditions, and constitutive properties (e.g., boundary conditions can be obtained from MRI measurements of blood flow [2]). Anatomic data is assembled as a solid model defined using Computer-Aided Design (CAD) tools whereas the physiologic model information is stored in the terms of attributes using an attribute management system [15], where both are housed under a simulation model manager [16]. Such an abstract definition, as provided by the simulation model manager, of the physical problem to be simulated is required for an automatic adaptive analysis environment.

The next stage in the overall process is to apply an appropriate numerical method to perform the simulation. To carry the process in an adaptive manner a feedback control loop is constructed. In each iteration of the feedback loop, flow computations are performed over an existing discretization followed by the determination of improvements required in the discretization to enhance the solution accuracy and execution of those improvements (e.g., see [13]). To advance the simulation in an automatic manner, the

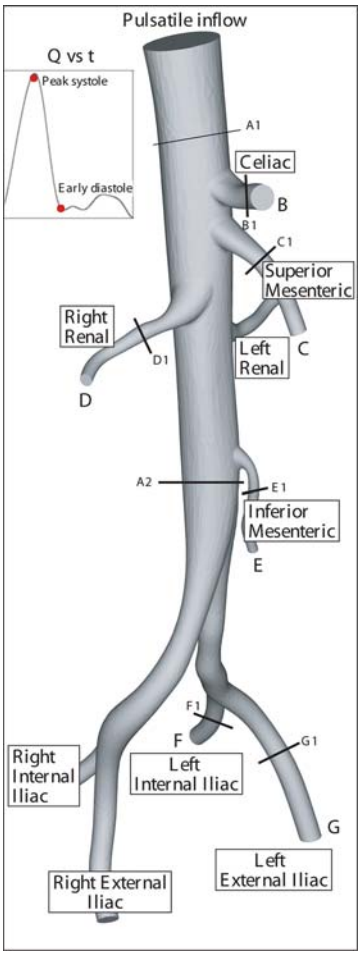

Fig. 1 Anatomic model of a healthy human abdominal aorta with various branches [14] along with labels for sections and outlets over which results are presented. Impedance boundary conditions [11], are prescribed at the outlets, that model the downstream vasculature bed to obtain physiologic flow conditions. The inset shows the volumetric flow rate at the inlet (the two *dots* in the inset correspond to instants of peak systole and early diastole)

adaptive control tools interact with each other in the loop and generate input data for the next set of flow computations.

The adaptive feedback process evaluates the quality of the computed solution, by using a posteriori error estimation and/or correction indication, on the current discretization to determine its suitability. With this information, errors associated with the discretization are controlled by locally improving the resolution. The key components of an automatic adaptive meshing method include:

- A posteriori error estimation/correction indication: estimating and/or obtaining an indication of the discretization error based on the quality of the computed solution (e.g., see [17, 18]).
- Mesh size field construction: transforming the information obtained in the above step into a mesh size field that describes the desired mesh resolution over the domain [13].
- Mesh modification strategy: altering the mesh based on the mesh size field information using local mesh modifications [19, 20] or global remeshing [21, 22].

In this article, we employ an anisotropic adaptive strategy to conform with the flow features, e.g., boundary layers that form near the vessel walls [13]. In order to incorporate directional information into the mesh size field, we rely on the Hessian strategy [23]. It is a suitable method when using linear finite elements, where second derivatives of the solution field are used to extract information on the error distribution. The Hessian can be computed from any component of the solution field. For example, a scalar field such as speed is usually chosen. In this study, we opt for the Hessian of the average flow speed over a cardiac cycle as a practical alternative for flows of pulsatile nature. The concept of mesh metric tensor [24], which defines a mapping of an ellipsoid in the physical space into a unit sphere in the *transformed/metric* space, is utilized to define the anisotropic mesh size field that prescribes the desired element size and orientation over the domain.

In case of blood flow simulations, more accurate results for key quantities of interest in regions of boundary layers, like wall shear stress, can be obtained with the help of

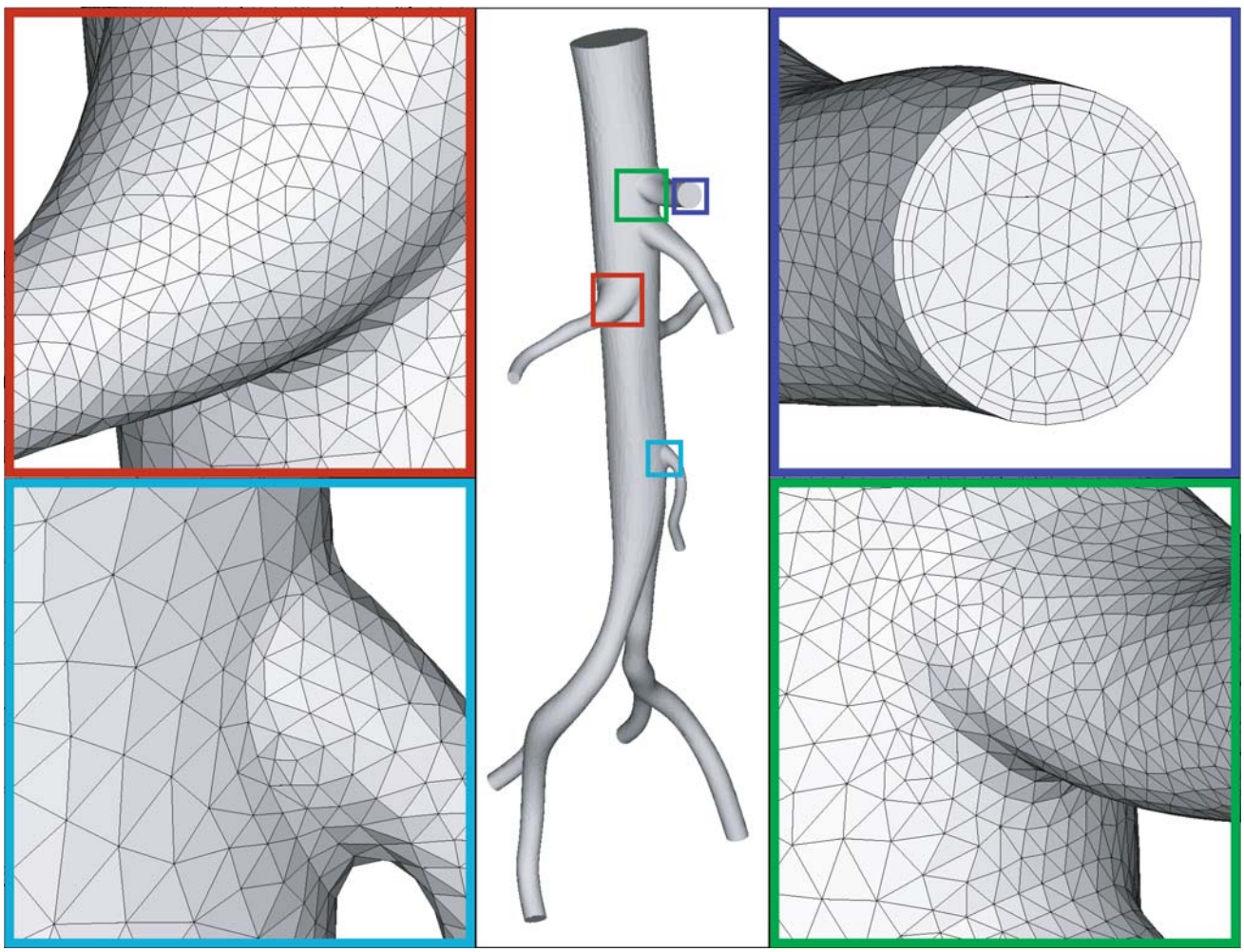

Fig. 2 Surface of the initial (pre-defined) boundary layer mesh (Mesh_{A0})

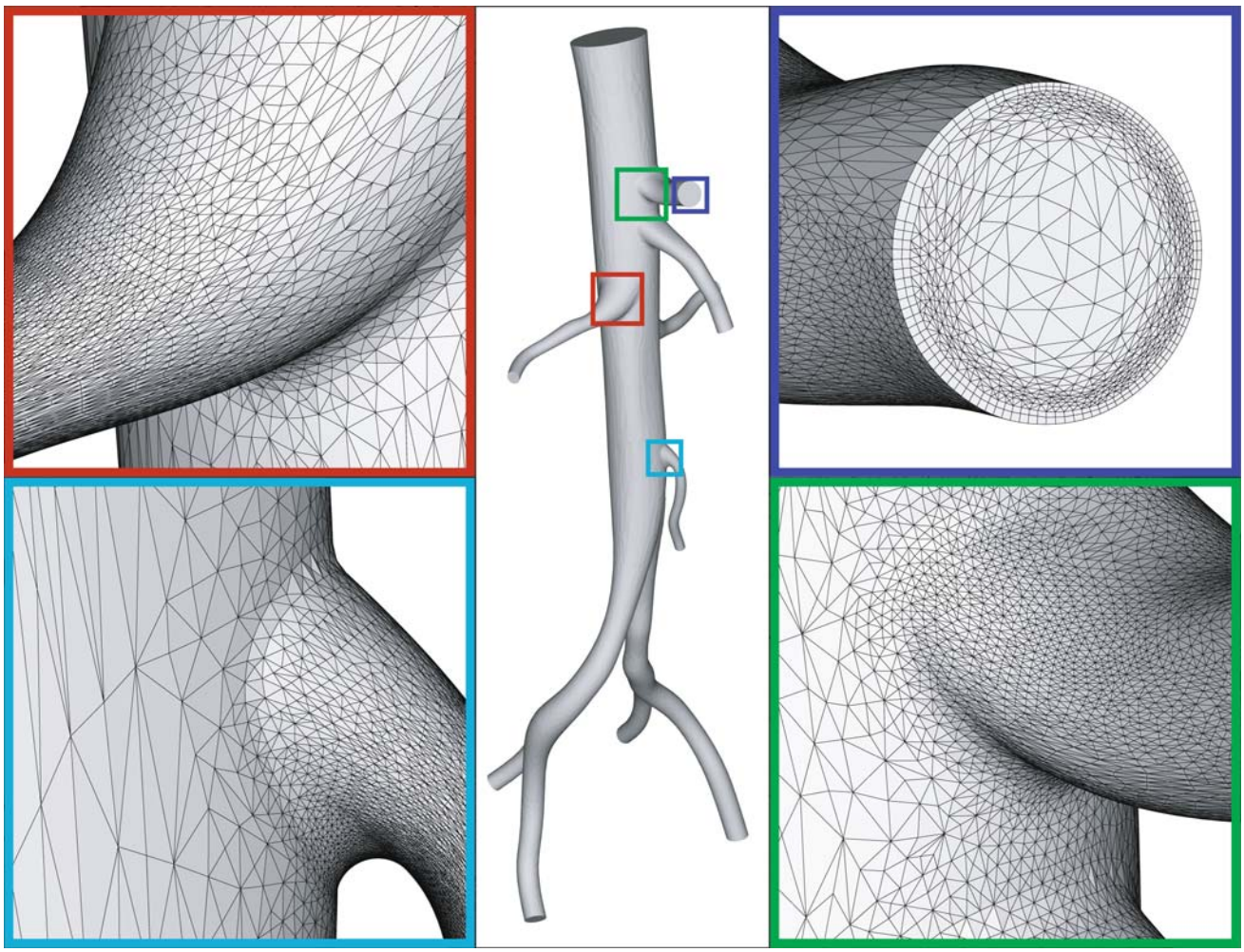

Fig. 3 Surface of the finest adapted boundary layer mesh (Mesh_{A3})

meshes with layered and graded elements near the vessel walls [13]. Such a mesh possesses structure in the direction normal to the walls due to creation of extruded layers of volume elements over unstructured surface mesh and is able to handle problems involving complex geometries and solution features. Favorable attributes of such meshes are high-aspect ratio, orthogonal, layered and graded elements at the walls for realistic geometries. Hence, in this study we employ the adaptive boundary layer meshing technique [25].

The adaptive flow solver can be summarized in the following steps. Flow computations are started on an initial discretization (pre-defined mesh) of the physical domain that is generated using an automatic boundary layer mesh generator [12] without any prior knowledge of the solution. Correction indicators are derived based on the computed solution that are used to dictate the mesh modification algorithm. Further, these steps are carried out in an iterative loop wherein improvements in the discretization are determined and realized.

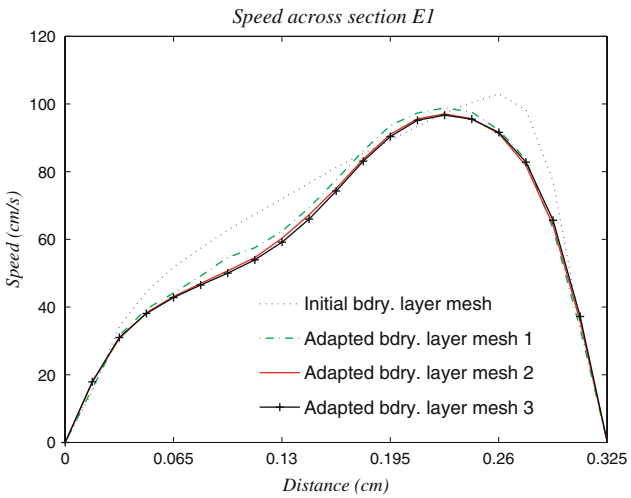

Fig. 4 Speed profiles for different boundary layer meshes across section E1 at early diastole

Table 1 Relative difference between speed profiles shown in Fig. 4 (finest adapted boundary layer mesh, Mesh_{A3}, with $1M$ nodes is considered as reference)

Mesh	Relative difference (Mesh_{A3} is ref.) (%)
Mesh_{A0} ($53k$ nodes)	11.8
Mesh_{A1} ($65k$ nodes)	3.9
Mesh_{A2} ($215k$ nodes)	1.0

More specifics of the numerical method utilized in this study are as follows. Flow computations are performed using a stabilized, semi-discrete finite element method for the transient, incompressible Navier–Stokes equation governing blood flow. In particular, we employ the streamline upwind/Petrov-Galerkin (SUPG) stabilization method introduced in [26] to discretize the governing equations. The stabilized finite element formulation currently utilized has been shown to be robust, accurate and stable on a variety of flow problems (see, e.g., [5, 27]). Linear finite elements, both for the pressure and the velocity fields, are used in these computations (note that equal-order interpolation for both fields is possible as SUPG stabilized formulation is employed). The system of non-linear ordinary differential equations obtained is discretized in time via a second-order generalized-α time integrator [28] resulting in a non-linear system of algebraic equations. This system is in turn linearized with Newton's method to obtain a linear algebraic system of equations that is solved using a custom linear algebra solver [29].

3 Results and discussion

The focus of this paper is on assessment and demonstration of the automated adaptive procedure to subject-specific anatomic models; specifically we now demonstrate the

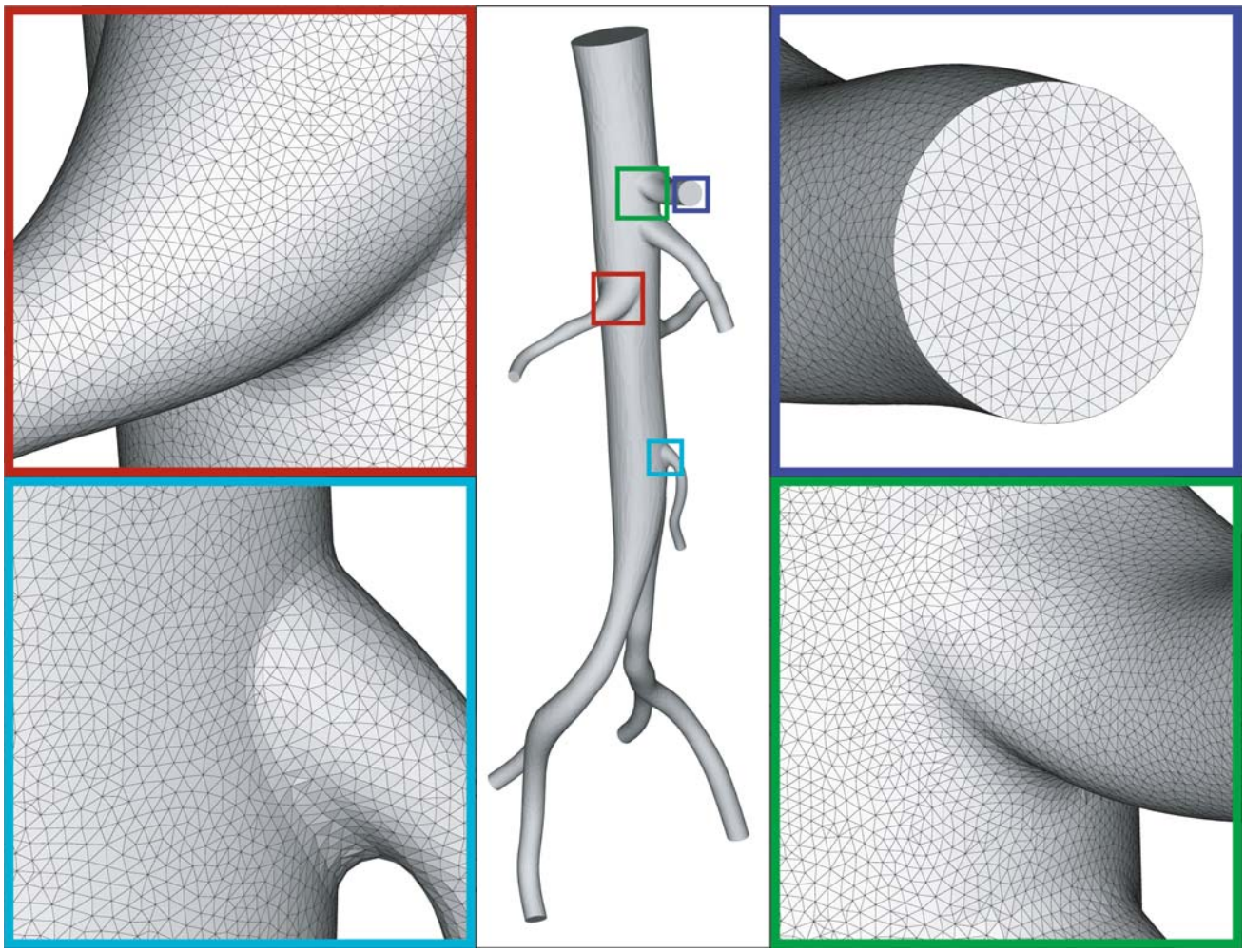

Fig. 5 Surface of a typical fully unstructured, globally uniform mesh, Mesh_{FU}, with a resolution that is selected to closely match the number of mesh nodes in the finest adapted boundary layer mesh shown in Fig. 3

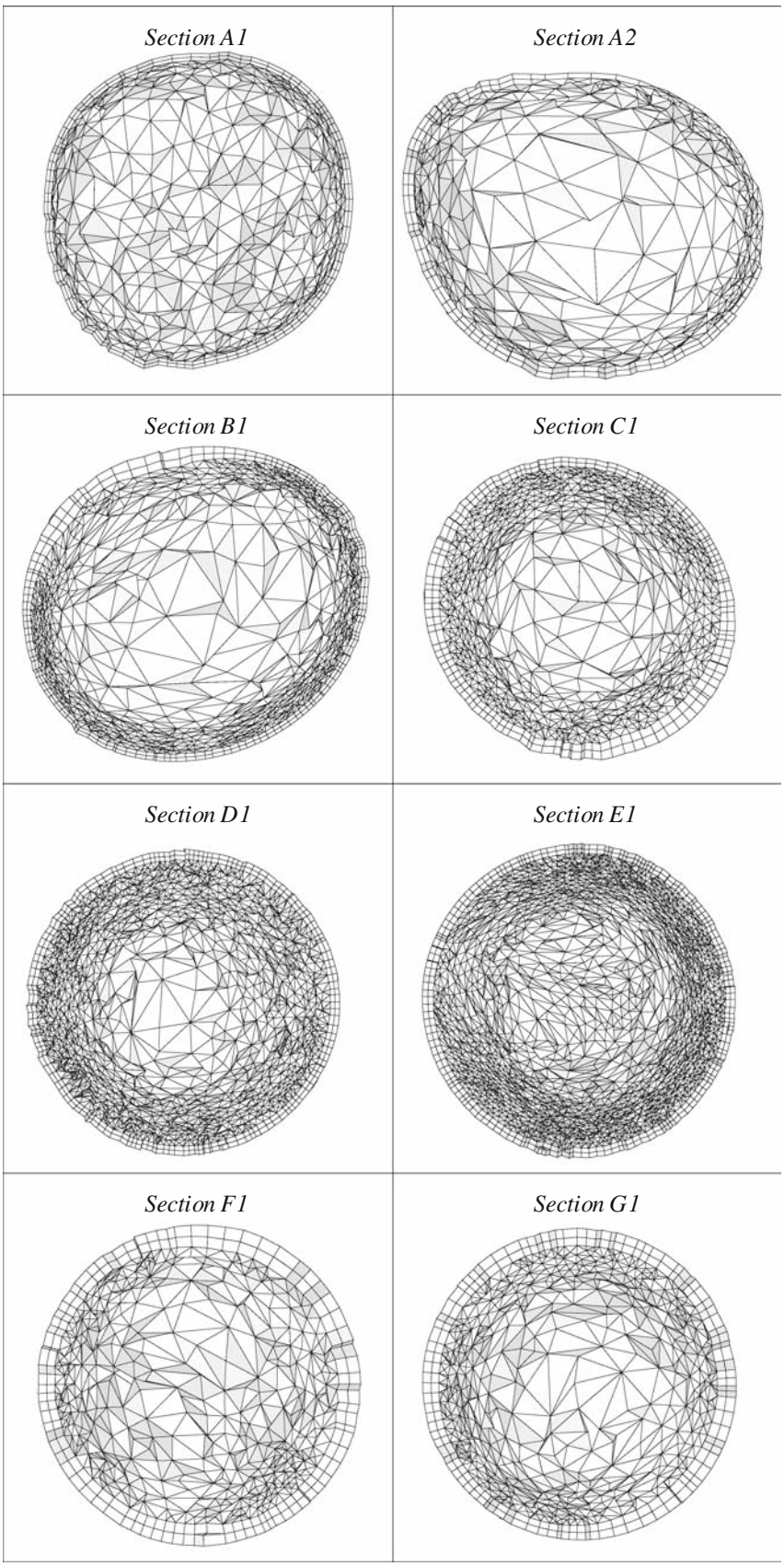

Fig. 6 Mesh faces cut by various sections (labeled in Fig. 1) through the finest adapted boundary layer mesh

application to a case of a human abdominal aorta of a normal subject with geometry and flow data collected from MRI. To this end, we present the features and characteristics of boundary layer mesh adaptivity by comparing two types of meshes: boundary layer meshes and fully unstructured, globally uniform mesh (without layered and graded elements near vessel walls). We first provide results obtained on subsequently adapted boundary layer meshes to illustrate convergence. We then present and compare results obtained on the finest adapted boundary layer mesh along with ones obtained on the fully, unstructured, globally uniform mesh. The results are provided in terms of spatial distribution of pressure and wall shear stress at two specific instants in the cardiac cycle; and temporal variations in flow rate and pressure at various outlets. Note that wall shear stress is a derived field that involves derivatives of the velocity field in its definition and is not as well resolved as pressure and velocity fields (see [13] for further details on its computation).

The layout of a healthy human abdominal aorta with various branches is shown in Fig. 1 along with labels for eight sections, i.e., A1, A2, B1, C1, D1, E1, F1, and G1, and 6 branch outlets, i.e., B, C, D, E, F, and G, over which results are presented. The main trunk is approximately 30 cm long with a diameter of 2.5 cm at the inlet (which is non-circular). The length of the branches varies from 1.8 to 5 cm whereas their diameter lies roughly between 0.3 and 0.8 cm. The waveform of the volumetric flow rate at the inlet is shown in the inset within Fig. 1, which is derived from the imaging data [14], with a time period t_p = 1.05 s; and a peak and trough of around 150 and 10 cc/s, respectively. The inset also shows two instants: peak systole, which is the heart contraction phase, and early diastole, which is the dilatation phase. No-slip conditions are assumed on the vessel walls and impedance boundary conditions are prescribed at the outlets [11] (where an electric circuit analog of an impedance, i.e., a measure of opposition to motion by a

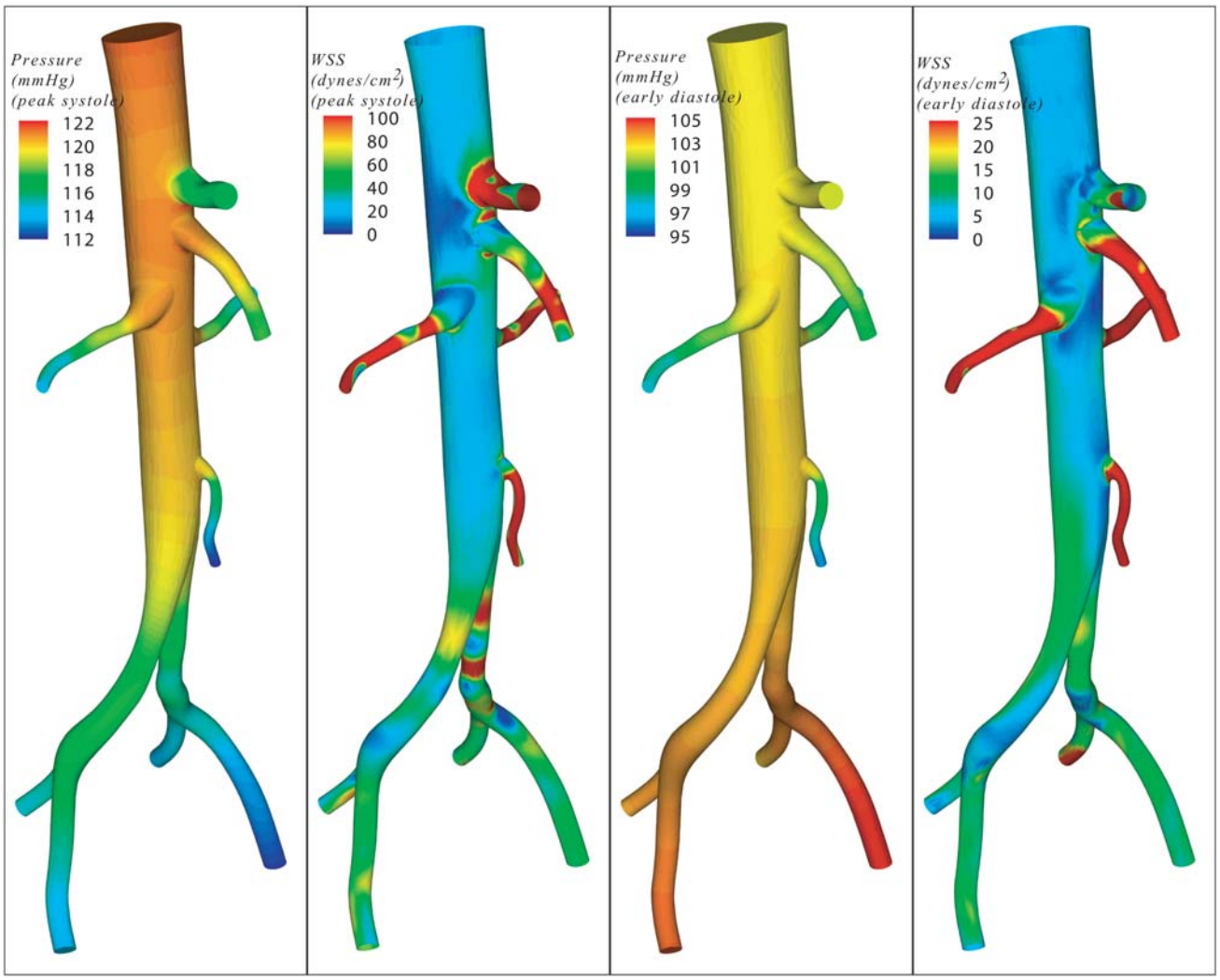

Fig. 7 Surface distribution of pressure and wall shear stress magnitude over vessel walls obtained on the finest adapted boundary layer mesh at peak systole and early diastole. Note: 1 mmHg = 133.3 Pa = 133.3 N/m^2 and 1 dyne/cm^2 = 0.1 Pa = 0.1 N/m^2

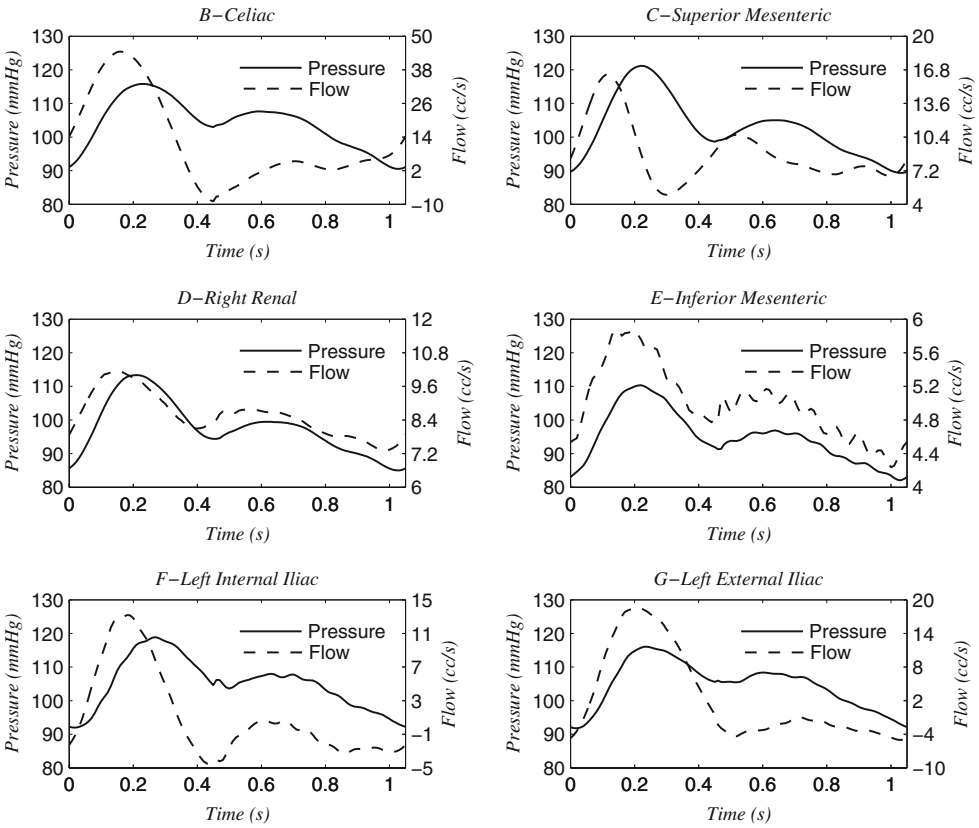

Fig. 8 Pressure and volumetric flow rate computed on the finest adapted boundary layer mesh at various outlets (labeled in Fig. 1). Note: 1 mmHg = 133.3 Pa = 133.3 N/m^2 and 1 cc/s = 10^{-6} m^3/s

system, is applied to relate downstream pressure with the flow rate). The viscosity and density are assumed to be $\mu =$ 0.04 dyne s/cm^2 and $\rho =$ 1.06 g/cm^3, respectively.

In this case, five cardiac cycles are simulated to obtain a periodic flow in time and thus, results for the last cardiac cycle are presented. Computations are performed using 105 time steps with equal time step size of 0.01 s in a cardiac cycle. The computations are started using an initial (pre-defined) boundary layer mesh, with two layers of constant thickness (normal resolution) and an isotropic interior volume mesh, consisting of approximately 53k nodes and 200k elements (where k denotes a thousand), see Fig. 2, and referred as Mesh$_{A0}$.

As mentioned before, a single mesh adaptation process is applied for the whole cardiac cycle. The average speed obtained over the last cardiac cycle is used to compute the correction indicators based on the Hessian strategy (see [13] for more details). Three iterations of the flow computation and mesh adaptation are performed to obtain a finest adapted boundary layer mesh (Mesh$_{A3}$) with around 1M nodes and 4.7M elements (where M denotes a million), see Fig. 3.

Speed profiles obtained on subsequently adapted boundary layer meshes across a diameter of section E1 at an instant of early diastole are shown in Fig. 4 to illustrate convergence. The relative difference between speed profiles (shown in Fig. 4) computed on the last two adapted boundary layer meshes is insignificant, even though the increase in number of nodes is by a factor of around 4.65, which indicates convergence, see Table 1 (where labels, Mesh$_{A1}$ and Mesh$_{A2}$, are used for intermediate adapted boundary layer meshes).

The effect of the flow features can be clearly seen on the finest adapted boundary layer mesh (see Fig. 3). The distribution of mesh resolution due to boundary layer mesh adaptivity conforms to the requirements of the solution as mesh elements are finer in regions of complex flow and coarser in other portions of the domain. Another crucial attribute to be noted is that boundary layer mesh adaptivity creates well aligned anisotropic elements, in areas with flow anisotropy, which accounts for the directionality of flow features. Moreover, it can be seen that boundary layer mesh adaptivity maintains layered and graded elements near the walls which incorporate mesh resolution as requested by correction indicators based on the computed flow (see Fig. 3).

In Fig. 5 a typical fully unstructured, globally uniform mesh (without layered and graded elements near vessel walls), referred as Mesh$_{FU}$, is shown for comparison in order to illustrate the outcome of mesh adaptation. The number of mesh nodes in case of the equi-resolution mesh has been chosen to be similar to the finest adapted boundary layer mesh, i.e., around 1M nodes, to give a clear impression of the resolution that would be available without using adaptivity. While this is the approach most

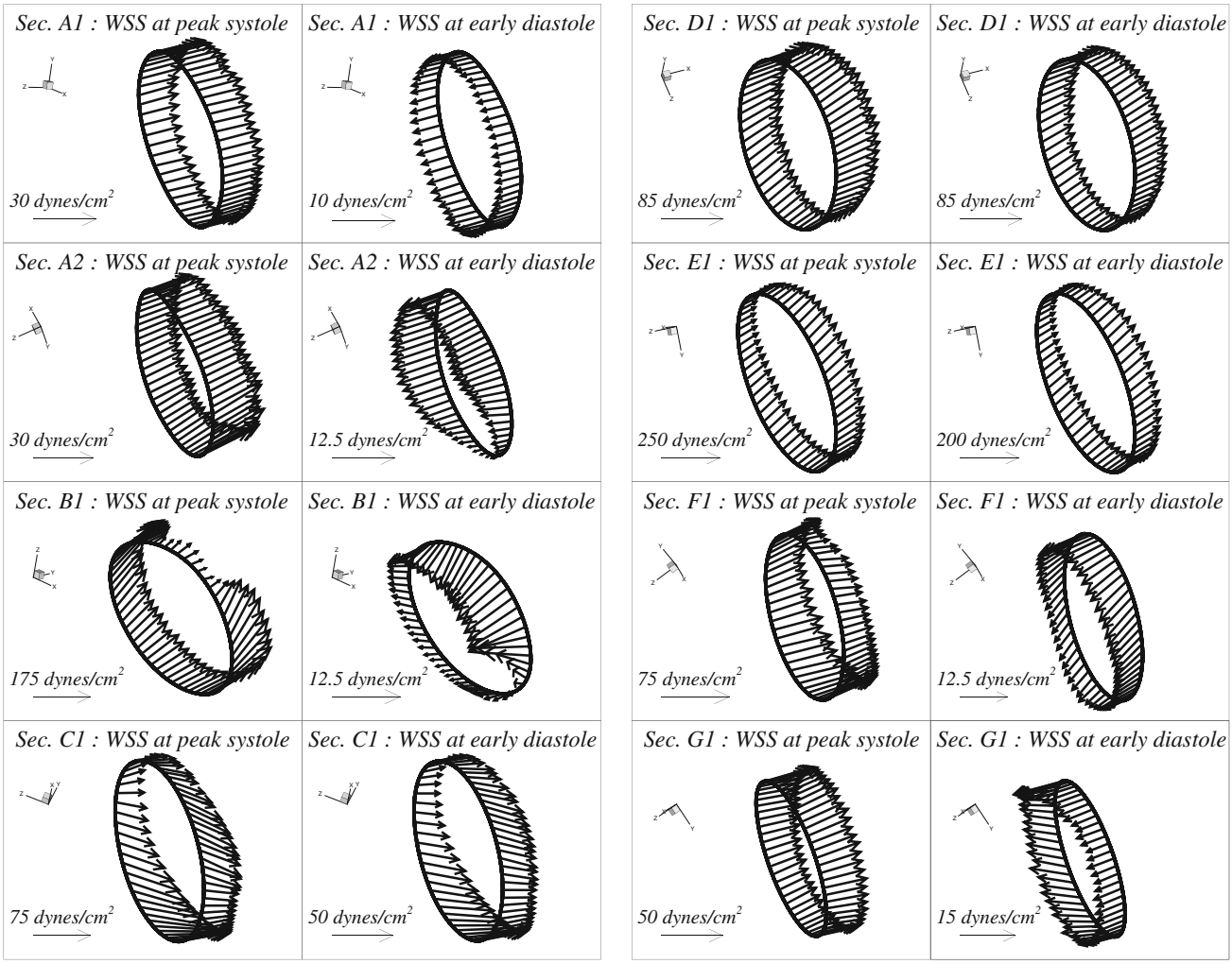

Fig. 9 Shear traction vectors computed on the finest adapted boundary layer mesh along the circumference of various sections (labeled in Fig. 1) at peak systole and early diastole. Note: 1 dyne/cm^2 = 0.1 Pa = 0.1 N/m^2

commonly used in current research (given the difficulty of estimating a priori the mesh size requirements in such a complicated flow), it is clear that automated boundary layer mesh adaptivity offers a better alternative. Later in this section we show that it leads to more accurate predictions with similar number of mesh nodes.

A magnified view of the finest adapted boundary layer mesh near the outlet of the celiac artery (top right window) in Fig. 3 shows the variation in mesh resolution along different directions, i.e., in axial, azimuthal and radial directions. Figure 6 provides additional evidence to support this observation where we present clip-plane view, i.e., a collection of mesh faces cut by a physical plane, of the finest adapted boundary layer mesh at various sections labeled in Fig. 1. Note that the quadrilateral faces near the vessel walls are due to boundary layer elements. The mesh resolution in each section is significantly different from others depending on the local flow features that vary in terms of shape and intensity over the domain. Isotropic elements are created where variation in flow is relatively similar in different directions, especially near the branching regions as shown in Fig. 3, reflecting the fact that the solution behavior is isotropic around such regions since the flow is not fully developed.

By comparing the initial boundary layer mesh (see Fig. 2) with the finest adapted boundary layer mesh (see Fig. 3); it can be seen that the geometric approximation is improved as the mesh resolution is increased [25, 30]. Other key features to be observed in adaptive boundary layer meshing are the azimuthal variation of layer thicknesses (normal resolution) and smooth transition of elements at the interface between the layered part and the interior tetrahedral part of the mesh, as illustrated by clip-plane views at various sections in Fig. 6.

To give a view of the flow patterns, results obtained on the finest adapted boundary layer mesh are presented in the form of distribution for pressure, volumetric flow rate and wall shear stress. Figure 7 displays the distribution of

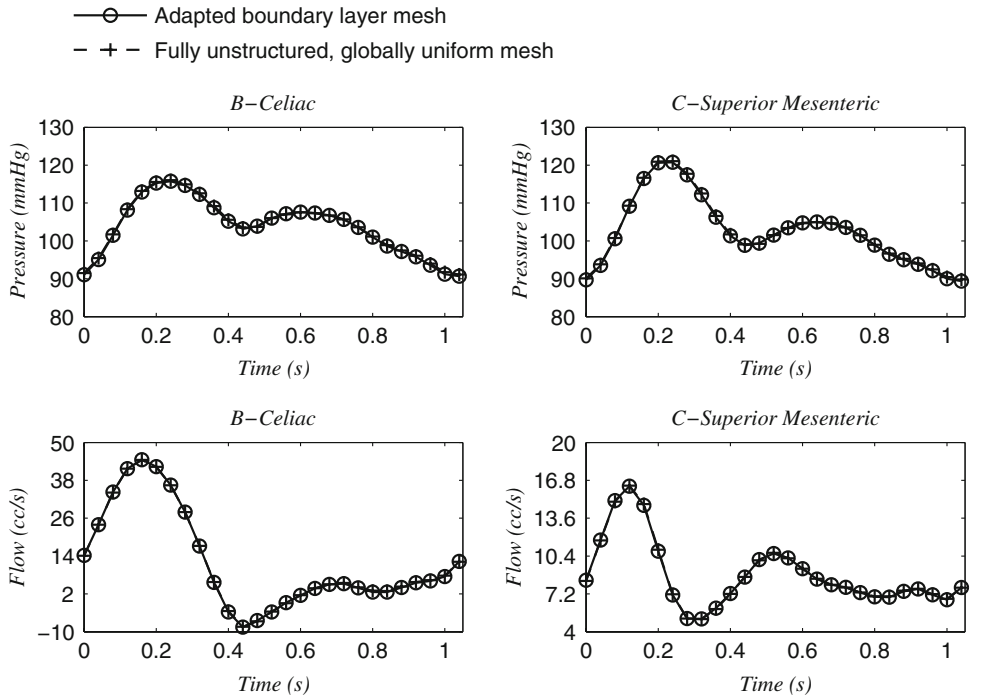

Fig. 10 Comparison of pressure and volumetric flow rate computed on the finest adapted boundary layer mesh and fully unstructured, globally uniform mesh at two outlets, celiac and superior mesenteric (as depicted in Figure 1). Note: 1 mmHg = 133.3 Pa = 133.3 N/m^2 and 1 cc/s = 10^{-6} m^3/s

pressure and wall shear stress magnitude over the vessel walls at two instants of the cardiac cycle. Figure 8 shows temporal variation of pressure and flow rates at various outlets.

Shear traction vectors, i.e., the tangential component of the surface traction acting on the wall, computed on the finest adapted boundary layer mesh are shown for various sections at two instants of the cardiac cycle in Fig. 9 (note that the length of the vectors are based on their magnitude and the isolated horizontal vector in each view is the reference vector). Variations seen in azimuthal component of wall shear stress are due to swirling flows that are typical in the cardiovascular system. The shear traction vectors shown in Fig. 9 at two time instants are in opposite directions for sections, A1, A2, B1, F1, and G1, indicating reverse flow. Reverse flow can also be observed in volumetric flow rate waveforms for outlets, B, F and G, shown in Fig. 8 after early flow deceleration phase of the cardiac cycle.

Figures 10 and 11 provide a comparison of the results obtained on the finest adapted boundary layer mesh to ones obtained on the fully unstructured, globally uniform mesh. Temporal variations in pressure and flow rate at two outlets, celiac and superior mesenteric (as depicted in Fig. 1), for both the meshes are indistinguishable, see Fig. 10. Clear differences can be seen in wall shear stress values computed on both the meshes in Fig. 11, which provides the distribution of pressure and wall shear stress over portions of vessel walls at peak systole. Figure 11 also shows shear traction vectors along two sections, B1 and E1, at peak systole and early diastole, respectively. This figure clearly illustrates that the wall shear stress is more difficult to resolve and therefore greatly benefits from boundary layer mesh adaptivity (e.g., complex spatial features captured without the spurious fluctuations observed in the fully unstructured, globally uniform mesh).

Profiles of wall shear stress magnitude computed on subsequently adapted boundary layer meshes along circumferential band at section E1 during early diastole indicate convergence on the finest one (see left plots in Fig. 12). Comparison of wall shear stress profiles at same location computed on the finest adapted boundary layer mesh against one obtained on the fully unstructured, globally uniform mesh (see right plots in Fig. 12) clearly demonstrates the spurious fluctuations obtained in the latter mesh without layered and graded elements near the vessel walls. This observation is reinforced with Table 2, which provides the relative difference for wall shear stress profiles (shown in Fig. 12). Table 3 demonstrates the degree of spurious fluctuations on different meshes, where maximum values for wall shear stress magnitudes along section E1 are provided along with relative difference in them. The results obtained show that physiological parameters like pressure and flow rates can be obtained accurately on fully unstructured, globally uniform meshes, perhaps coarser meshes, whereas key quantities of interest like wall shear stress requires boundary layer mesh adaptivity.

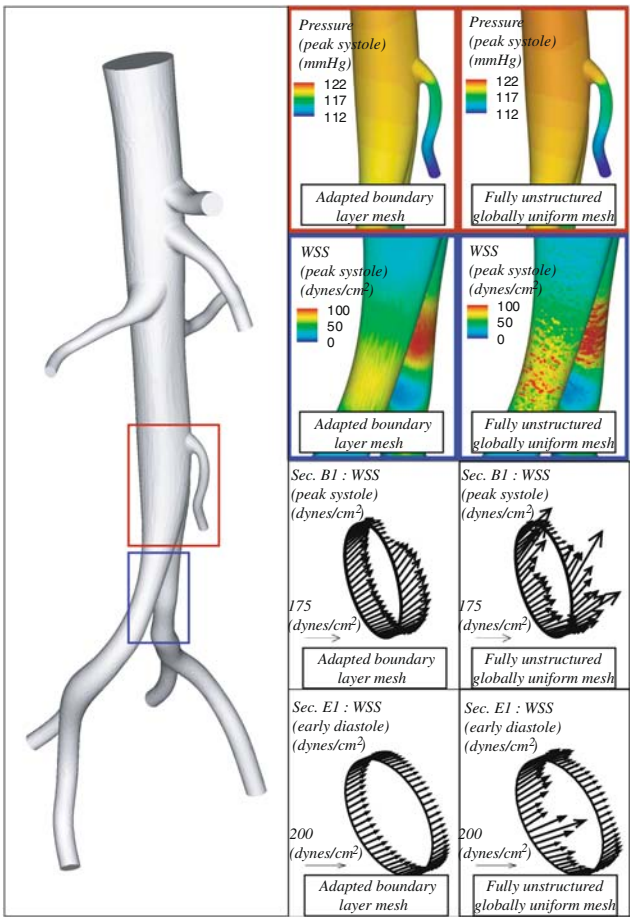

Fig. 11 Comparison of pressure and wall shear stress over portions of vessel walls obtained on the finest adapted boundary layer mesh and fully unstructured, globally uniform mesh at peak systole and early diastole. Note: 1 mmHg = 133.3 Pa = 133.3 N/m^2 and 1 dyne/cm^2 = 0.1 Pa = 0.1 N/m^2

4 Closing remarks

In this study, we have presented an automatic adaptive procedure to perform blood flow simulations in the cardiovascular system. We first described the overall adaptive procedure that can be initiated for a subject based on the clinical measurements obtained from MRI. We then provided the key components of an adaptive meshing method.

We showed the capabilities of the adaptive procedure by applying it to a model of a human abdominal aorta of a normal subject. We further demonstrated the features and characteristics of an adaptive boundary layer meshing technique that incorporates the capability to maintain layered and graded elements near the vessel walls. We showed convergence on the finest adapted boundary layer mesh. We also provided and compared the results obtained on the adapted boundary layer meshes and fully unstructured, globally uniform mesh in the form of spatial distribution

Table 2 Relative difference between wall shear stress profiles shown in Fig. 12 (finest adapted boundary layer mesh, Mesh$_{A3}$, with 1*M* nodes is considered as reference)

Mesh	Relative difference (Mesh$_{A3}$ is ref.) (%)
Mesh$_{A0}$ (53*k* nodes)	13.9
Mesh$_{A1}$ (65*k* nodes)	4.5
Mesh$_{A2}$ (215*k* nodes)	2.1
Mesh$_{FU}$ (1*M* nodes)	29.5

Table 3 Maximum values for wall shear stress magnitude along section E1 on different meshes along with relative difference in the maximum

Mesh	Maximum value (dyne/cm^2)	Relative difference in maximum (Mesh$_{A3}$ is ref.) (%)
Mesh$_{A0}$ (53*k* nodes)	158.95	27.1
Mesh$_{A1}$ (65*k* nodes)	138.88	11.1
Mesh$_{A2}$ (215*k* nodes)	123.80	1.0
Mesh$_{A3}$ (1*M* nodes)	125.03	–
Mesh$_{FU}$ (1*M* nodes)	291.40	133.1

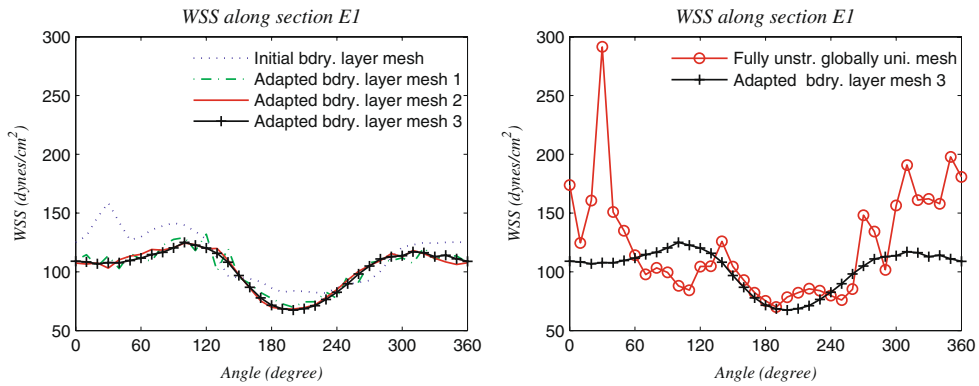

Fig. 12 Comparison of wall shear stress magnitude computed on subsequently adapted boundary layer meshes and fully unstructured, globally uniform mesh along section E1

for pressure and wall shear stress, and temporal variations in flow rate and pressure at various outlets. The results obtained clearly show that boundary layer mesh adaptivity offers a better alternative leading to more accurate predictions with similar number of mesh nodes, especially for key physiological quantities like wall shear stress.

Acknowledgments We gratefully acknowledge the support of this work by NSF grants ACI-0205741 and 0749152. We would also like to acknowledge that some of the computations carried in this study were performed on parallel computers obtained through NSF grant 0420703. The results presented in this article made use of the linear algebra library provided by ACUSIM Software Inc. The attribute management system used in this study was provided by Simmetrix Inc.

References

1. Ku DN (1997) Blood flow in arteries. Annu Rev Fluid Mech 29:399–434
2. Taylor CA, Draney MT (2004) Experimental and computational methods in cardiovascular fluid mechanics. Annu Rev Fluid Mech 36:197–231
3. Perktold K, Resch M, Peter RO (1991) Three-dimensional numerical analysis of pulsatile flow and wall shear stress in the carotid artery bifurcation. J Biomech 24:409–420
4. Moore JA, Rutt BK, Karlik SJ, Yin K, Ethier CR (1999) Computational blood flow modeling based on in vivo measurements. Ann Biomed Eng 27:627–640
5. Taylor CA, Hughes TJR, Zarins CK (1998) Finite element modeling of blood flow in arteries. Comput Meth Appl Mech Eng 158:155–196
6. Taylor CA, Draney M, Ku J, Parker D, Steel B, Wang K, Zarins C (1999) Predictive medicine: computational techniques in therapeutic decision-making. Comput Aided Surg 4 (5):231–247
7. Stuhne GR, Steinman DA (2004) Finite-element modeling of the hemodynamics of stented aneurysms. Trans. ASME J Biomech Eng 126(3):382–387
8. Steinman DA, Taylor CA (2005) Flow imaging and computing: large artery hemodynamics. Ann Biomed Eng 33 (12):1704–1709
9. Friedman MH, Giddens DP (2005) Blood flow in major blood vessels-modeling and experiments. Ann Biomed Eng 33(12): 1710–1713
10. Figueroa CA, Vignon-Clementel IE, Jansen KE, Hughes TJR, Taylor CA (2006) A coupled momentum method for modeling blood flow in three-dimensional deformable arteries. Comput Meth Appl Mech Eng 195:5685–5706
11. Vignon-Clementel IE, Figueroa CA, Jansen KE, Taylor CA (2006) Outflow boundary conditions for three-dimensional finite element modeling of blood flow and pressure in arteries. Comput Meth Appl Mech Eng 195:3776–3796
12. Garimella RV, Shephard MS (2000) Boundary layer mesh generation for viscous flow simulations. Int J Numer Meth Eng 49:193–218
13. Sahni O, Müller J, Jansen KE, Shephard MS, Taylor CA (2006) Efficient anisotropic adaptive discretization of the cardiovascular system. Comput Meth Appl Mech Eng 195:5634–5655
14. Tang BT, Cheng CP, Draney MT, Wilson NM, Tsao PS, Herfkens RJ, Taylor CA (2006) Abdominal aortic hemodynamics in young healthy adults at rest and during lower limb exercise: quantification using image-based computer modeling. Am J Physiol Heart Circ Physiol 291(2):H668–H676
15. O'Bara RM, Beall MW, Shephard MS (2002) Attribute management system for engineering analysis. Eng Comput 4:339–351
16. Shephard MS, Beall MW, O'Bara RM, Webster BE (2004) Toward simulation-based design. Finite Elem Anal Des 40:1575–1598
17. Ainsworth M, Oden JT (2000) A posteriori error estimation in finite element analysis. Wiley, New York
18. Verfürth R (1996) A review of posteriori error estimation and adaptive mesh-refinement techniques. Teubner-Wiley, Stuttgart
19. Bänsch E (1991) Local refinements in 2 and 3 dimensions. Impact Comput Sci Eng 3:181–191
20. de Cougny HL, Shephard MS (1999) Parallel refinement and coarsening of tetrahedral meshes. Int J Numer Meth Eng 46:1101–1125
21. George P-L, Borouchaki H, Laug P (2002) An efficient algorithm for 3D adaptive meshing. Adv Eng Softw 33:377–387
22. George P-L (1999) Tet meshing: construction, optimization and adaptation. In: Proceedings of eighth international meshing roundtable, South Lake Tao
23. Kunert G (2002) Toward anisotropic mesh construction and error estimation in the finite element method. Numer Methods Partial Differ Equ 18:625–648
24. Borouchaki H, George P-L, Mohammadi B (1997) Delaunay mesh generation governed by metric specifications. Part II. Applications. Finite Elem Anal Des 25:85–109
25. Sahni O, Jansen KE, Shephard MS, Taylor CA, Beall MW (2008) Adaptive boundary layer meshing for viscous flow simulations. Eng Comput 24:267–285
26. Brooks AN, Hughes TJR (1982) Streamline upwind/Petrov–Galerkin formulations for convection dominated flows with particular emphasis on the incompressible Navier–Stokes equations. Comput Meth Appl Mech Eng 32:199–259
27. Whiting CH, Jansen KE (2001) A stabilized finite element method for the incompressible Navier–Stokes equations using a hierarchical basis. Int J Numer Meth Fluids 35:93–116
28. Jansen KE, Whiting CH, Hulbert GM (1999) A generalized-α method for integrating the filtered Navier–Stokes equations with a stabilized finite element method. Comput Meth Appl Mech Eng 190:305–319
29. Shakib F http://www.acusim.com
30. Li X, Shephard MS, Beall MW (2003) Accounting for curved domains in mesh adaptation. Int J Numer Meth Eng 58:247–276